Supplementary Information

Synergistic effect of Ag-doped Mn_3O_4 and AgCl composite as a regenerable and high-performance catalyst for the oxygen reduction reaction

Anagha Yatheendran,[a] Aswathy M Narayanan,[b] Jeetu S. Babu[c], Rahul Rajan[a] and N. Sandhyarani*[a]

[a]Nanoscience Research Laboratory, Department of Materials Science and Engineering, National Institute of Technology Calicut, Calicut, Kerala, India, Fax: 91 495 2287250, Tel.: 91 495 2286537, * E-mail: sandhya@nitc.ac.in

[b]Department of Chemistry, Vel Tech Rangarajan Dr. Sagunthala R&D Institute of Science and Technology, 400 feet outer ring road, Avadi, Chennai, Tamil Nadu 600062

[c] Department of Materials Science and Engineering, National Institute of Technology Calicut, Calicut, Kerala, India, Fax: 91 495 2287250

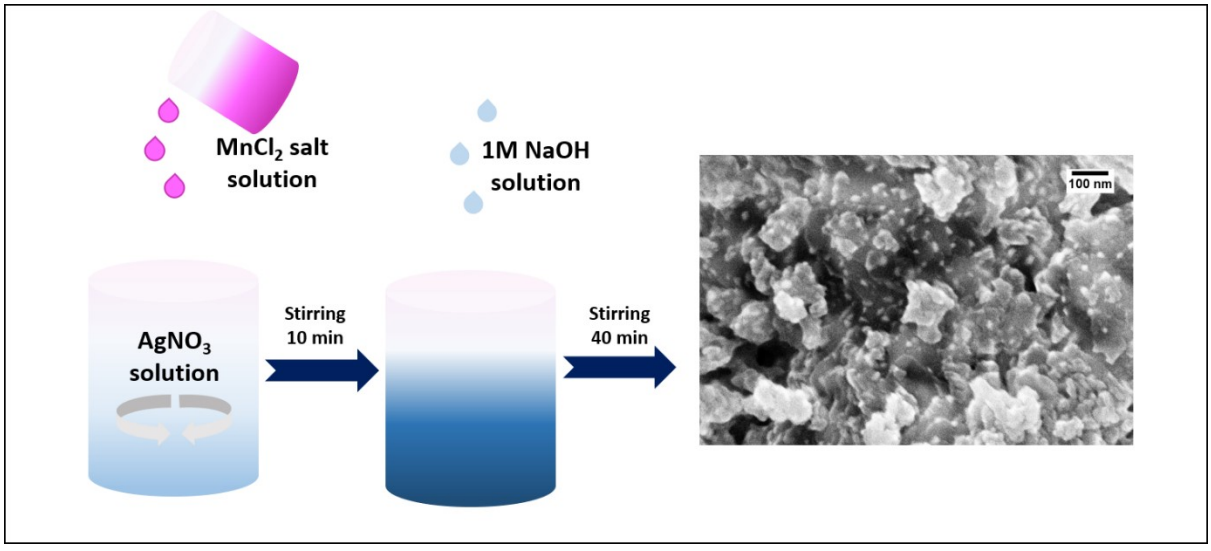

Fig. S1 Schematic of the synthesis of AgCl-Ag:Mn_3O_4

Synthesis of Ag- Mn_3O_4 (Bulk)

Bulk Ag- Mn_3O_4 was synthesized through the ex-situ treatment of separately synthesized Ag and Mn_3O_4 in a 4:1 ratio (the same ratio in the AgCl-Ag:Mn_3O_4). Ag was derived through the calcination of Ag_2O at 400 ℃ for two h.

Synthesis of AgNp-Mn_3O_4 (Nano)

AgNp-Mn_3O_4 (Nano) was obtained through the ex-situ treatment of separately synthesized silver nanoparticles and Mn_3O_4 in a 4:1 ratio. To synthesize silver nanoparticles, A 10-mL of 1.0 mM silver nitrate was prepared and added dropwise to 30 mL of 2.0 mM sodium borohydride solution chilled in an ice bath under vigorous stirring conditions. The solution initially turned light yellow and then brighter yellow after adding silver nitrate. Then, the sample was collected after centrifugation, mixed with Mn_3O_4 (0.4 mg), and stirred further for 40 min. The final sample is collected after centrifugation and dried at 70 ℃.

Synthesis of Mn_3O_4

The manganese oxide Mn_3O_4 was synthesized through the coprecipitation method. 0.025 M manganese (II) chloride solution were prepared, followed by stirring for 10 min. The pH of 10 was adjusted with the addition of 1 M NaOH. The solution was further stirred for 40 min, and the product was washed with water and ethanol sequentially. The final product was collected by drying at 80 ℃.

Synthesis of pristine AgCl

The pristine AgCl was prepared using the coprecipitation method with an equimolar mixture of $AgNO_3$ and NaCl.

Synthesis of AgCl- Mn_3O_4

To identify the role of synthetic conditions, the composite AgCl-Mn_3O_4 was prepared by two-step synthesis. AgCl and Mn_3O_4 were synthesized separately and mixed in a 4:1 ratio (to obtain the same ratio as the composite mentioned in this work). Pristine AgCl was prepared through the reaction with an equimolar mixture of $AgNO_3$ and NaCl, and Pristine Mn_3O_4 was prepared with the treatment of NaOH with Manganese (II) chloride precursor, as discussed in detail. XRD characterization confirmed the formation of AgCl and Mn_3O_4 within the system.

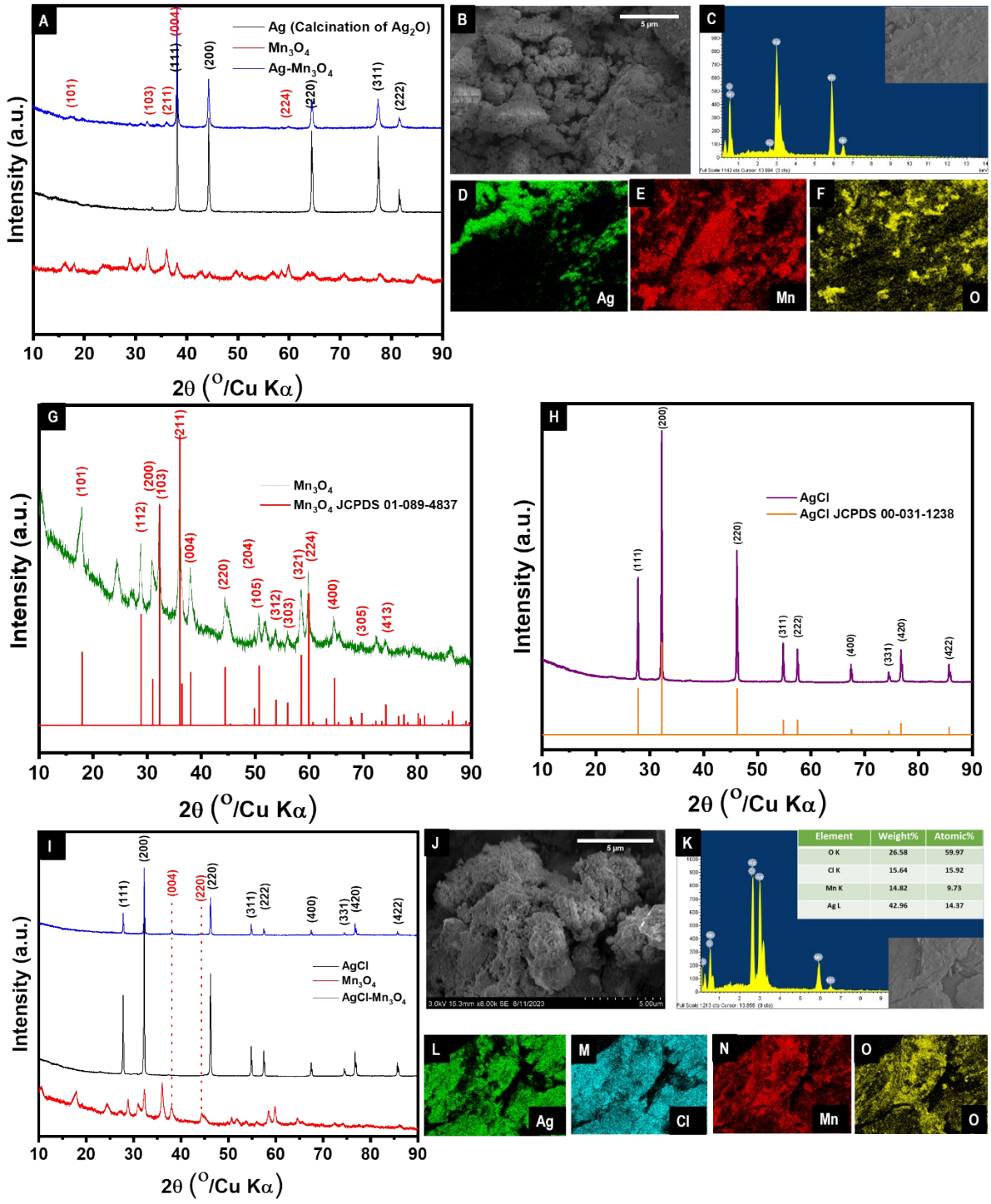

Fig.S2 XRD (A), SEM image (B), EDS spectrum and corresponding elemental mapping (C-F) of Ag-Mn_3O_4, XRD of Mn_3O_4 (G), and XRD of AgCl (H), XRD (I), SEM image (J), EDS spectrum and corresponding elemental mapping (K-O) of two-step derived AgCl-Mn_3O_4.

The occurrence of polydispersed nanosized particles was confirmed from the SEM, and elemental analysis was performed with EDS, establishing the presence of Ag, Mn, and O within

the composite. All the characteristic peaks corresponding to Ag and Mn_3O_4 were observed in the XRD spectrum of Ag-Mn_3O_4. Figure S2 G shows the XRD of Mn_3O_4. The peaks at 32.1°, 35.9°, 38°, 44.2°, 59.8°, and 64.3°, 74.3°, 76.6°, 85.6° can be assigned to tetragonal Mn_3O_4 planes (103), (211), (004), (220), (224), and (400), (413), (422) and (424) respectively. 32.1°, 74.3°,76.6°, and 85.6° can be further assigned to the (103), (413), (422), and (424) planes of Mn_3O_4, and the obtained result agrees with the JCPDS 01-089-4837.

In Figure S2 H, the presence of peaks at 27.7°, 32.1°, 46.1°, 54.7°, 57.3°, 67.3°, 74.3°, 76.6°, 85.6° can be assigned to the characteristic peaks of (111), (200), (220), (311), (222), (400), (331), (420), and (422) planes of cubic AgCl with space group Fm-3m. The obtained data greatly agree with the reported literature and JCPDS 00-031-1238.

The presence of Ag, Cl, Mn, and O were confirmed with EDS analysis, and uniform distribution of elements was observed in EDS mapping of AgCl-Mn_3O_4. Similarly, in XRD analysis, AgCl-Mn_3O_4 exhibited all the major characteristic peaks corresponding to AgCl and Mn_3O_4. The presence of peaks at 27.8°, 32.2°, 46.2°, 54.8°, 57.4°, 67.4°, 74.4°, 76.7°, 85.6° can be assigned to the characteristic peaks of (111), (200), (220), (311), (222), (400), (331), (420), and (422) planes of cubic AgCl and the obtained data greatly agree with the reported literature and JCPDS 00-031-1238.

AgCl (*Fm*-3*m*), a = 5.5500(6), Weight fraction 0.722(3), Residuals RF, RF^2 = 7.70%, 10.01%								
Atom	Type	x	y	z	Fractional occupancy	Site symmetry	Multiplicity	U_{iso}
Ag	Ag^{+}	0.0000	0.0000	0.0000	1.0	m3m	4	0.06966
Cl	Cl^{-}	0.5000	0.5000	0.5000	1.0	m3m	4	0.04053
Ag (*Fm*-3*m*), a = 4.0860,(3), Weight fraction 0.0829(1), Residuals RF, RF^2 = 7.21%, 16.88%								
Atom	Type	x	y	z	Fractional occupancy	Site symmetry	Multiplicity	U_{iso}
Ag	Ag^{+}	0.0000	0.0000	0.0000	1.0	m3m	4	0.0100
Ag doped Mn_3O_4 ($I4_1/amd$), a = 5.755(2), c = 9.489(6), Weight fraction 0.194(3), Residuals RF, RF^2 = 26.16%, 40.76%								
Atom	Type	x	y	z	Fractional occupancy	Site symmetry	Multiplicity	U_{iso}
Mn1	Mn^{+2}	0.0000	0.2500	0.8750	1.0	-4m2(z)	4	0.0100
Ag1	Ag^{+1}	0.0000	0.5000	0.5000	0.071	2/m(x)	8	0.0100
Mn2	Mn^{+3}	0.0000	0.5000	0.5000	0.929	2/m(x)	8	0.0100
O1	O^{-2}	0.0000	0.45662	0.26875	1.0	m(x)	16	0.0100

Table S1. Refinement results of AgCl, Ag, and Ag-doped Mn_3O_4 in the composite.

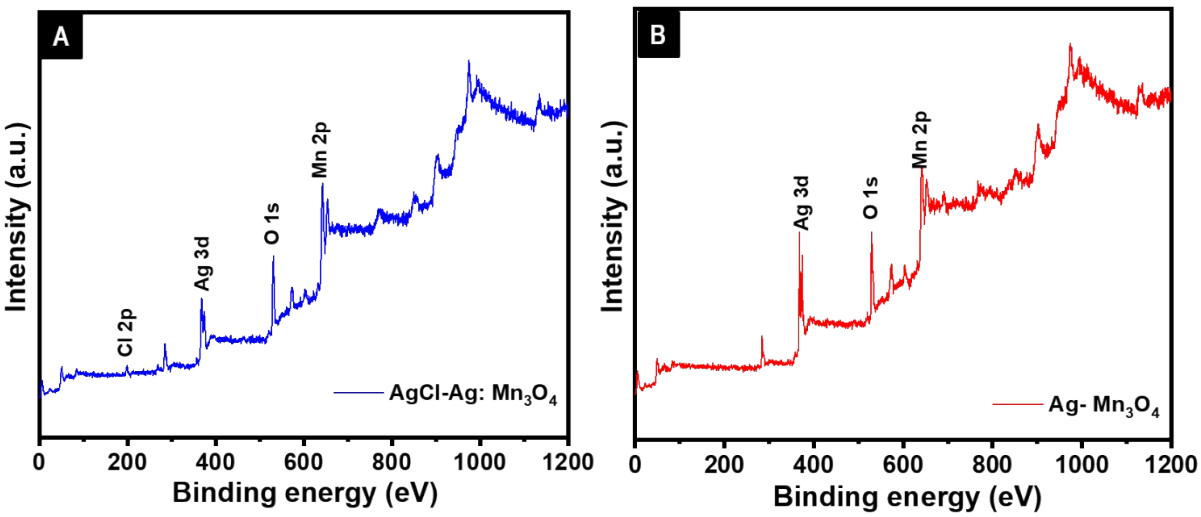

Fig. S3 XPS survey spectrum of AgCl-Ag:Mn_3O_4 (A), Ag-Mn_3O_4 (B)

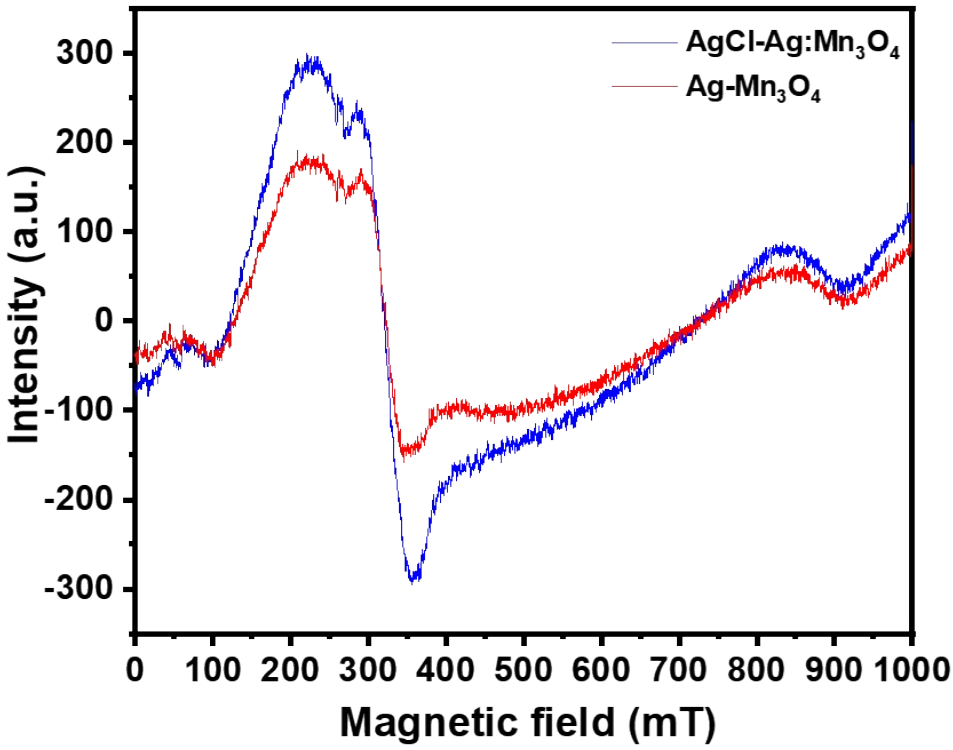

Fig. S4 EPR spectra of AgCl-Ag:Mn_3O_4 and Ag-Mn_3O_4

The existence of oxygen vacancy was further confirmed by an EPR analysis. g- values of 2.10 and 2.09 were observed for AgCl-Ag:Mn_3O_4, and Ag-Mn_3O_4, respectively. The peak intensity

observed was higher for AgCl-Ag:Mn_3O_4 than the Ag-Mn_3O_4 catalyst, suggesting more oxygen vacancies in AgCl-Ag:Mn_3O_4 in agreement with the XPS results.[1]

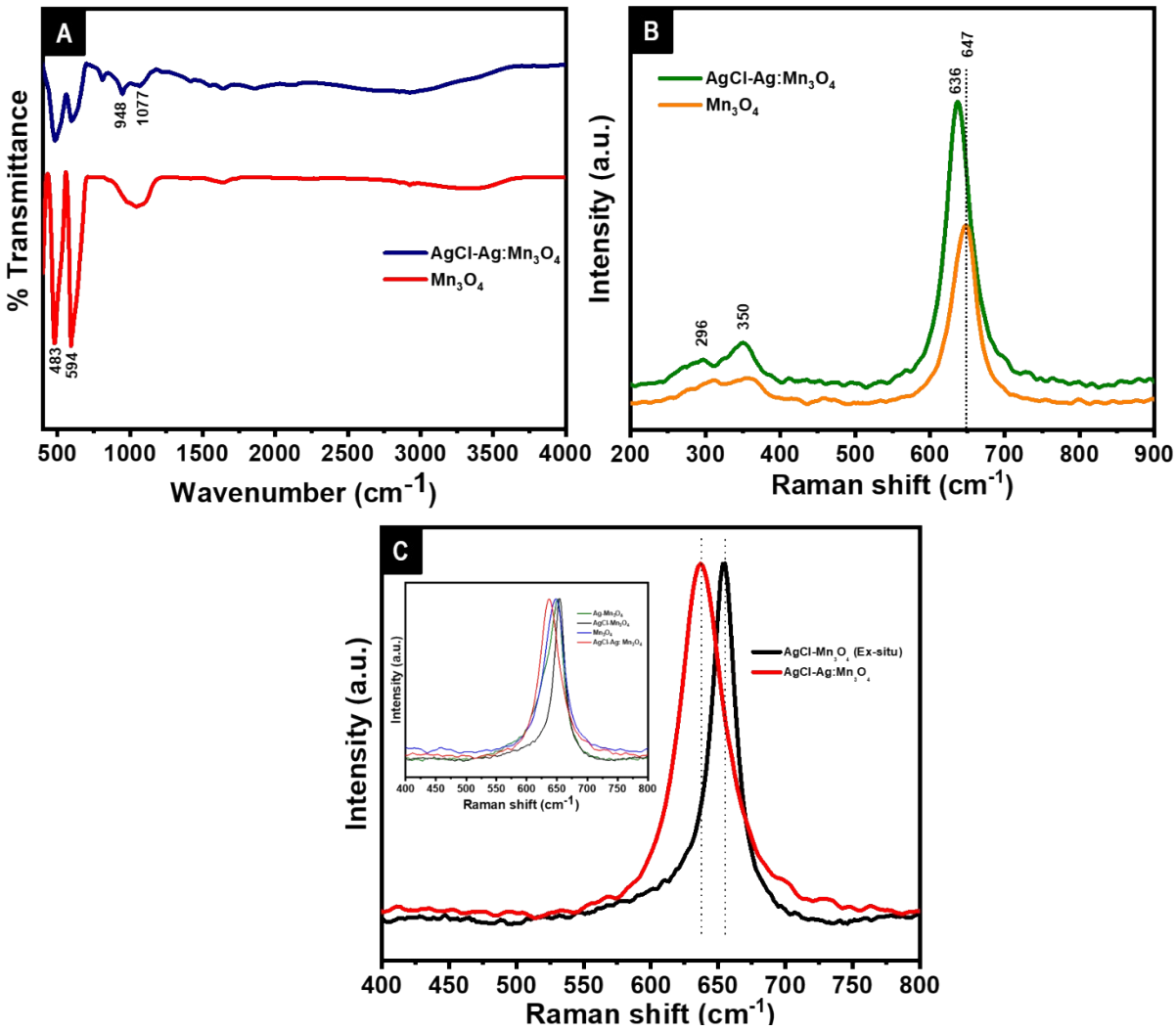

Fig. S5 FTIR (A), and Raman (B) spectra of Mn_3O_4 and AgCl-Ag:Mn_3O_4, and Raman (C) spectra of single-step derived AgCl-Ag:Mn_3O_4 and two-step synthesized AgCl-Mn_3O_4.

The FTIR spectrum in Figure S5 A shows peaks around 485 cm^{-1} and 594 cm^{-1}, which can be attributed to the coupling mode between the Mn-O stretching modes of octahedral and tetrahedral sites of Mn_3O_4. The peak around 594 cm^{-1} can also be assigned due to the excited lattice mode.[2-6]

Characteristic peaks in the Raman spectra shown in Figure S5 B around 647 cm^{-1}, 350 cm^{-1}, and 296 cm^{-1} confirm the formation of Mn_3O_4. These peaks correspond to the A_{1g}, T_{2g}, and E_g

modes of the Mn_3O_4.[7] The presence of a strong band at 647 cm^{-1} and two weak broad bands at 350 cm^{-1} and 296 cm^{-1} agree with the reported literature.[8] The strong peak of 647 cm^{-1} can be attributed to the A_{1g} mode of the Mn-O bond breathing vibration of manganese ions (divalent) at the tetrahedral coordination. The other smaller peaks located around 296 and 350 cm^{-1} can be assigned due to the combination of vibrations of tetrahedral and octahedral oxygen atoms.[9] The shift of 647 cm^{-1} peak in Mn_3O_4 to 636 cm^{-1} in AgCl-Ag: Mn_3O_4 indicates the structural distortion in Mn_3O_4 by the introduction of Ag doping. To study the effect of doping in detail, we performed Raman analysis in the in situ synthesized AgCl-Ag:Mn_3O_4 and two-step derived AgCl-Mn_3O_4, and the results obtained are shown in Figure S5 C. A visible shift was observed in the Raman spectrum of AgCl-Ag:Mn_3O_4 while comparing bare Ag-Mn_3O_4 (bulk), Mn_3O_4 alone, and two-step derived AgCl-Mn_3O_4 system, which supports the doping in AgCl-Ag:Mn_3O_4.

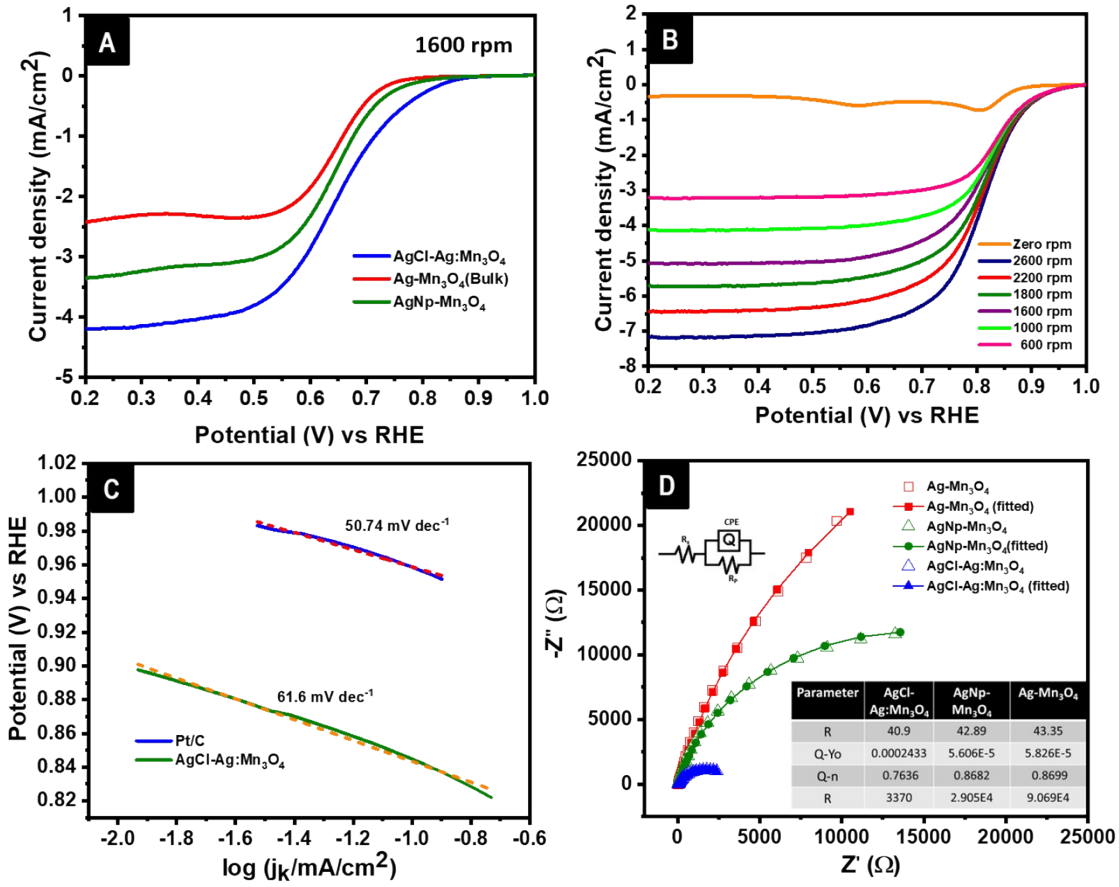

Fig. S6 Comparison of LSV of AgCl-Ag:Mn_3O_4 with Ag-Mn_3O_4 and AgNp-Mn_3O_4 (A), LSV of Pt/C (B), Tafel plots of the AgCl-Ag:Mn_3O_4 and Pt/C (C), and EIS of AgCl-Ag:Mn_3O_4 and Ag-Mn_3O_4 (D).

From the LSV and EIS, it is observed that the synergistic effect derived through the coprecipitation synthesis is responsible for the enhanced performance of the catalyst, and the role of AgCl in the augmented performance is also proved.

The performance of the catalyst is compared with benchmark Pt/C. The Tafel slope obtained from mass transport corrected LSV at 1600 rpm for the composite catalyst is compared with Pt/C, and it exhibited a Tafel slope of 50.74 mV/dec, and the catalyst AgCl-Ag:Mn_3O_4 showed a Tafel slope of 61.6 mV/dec, respectively, indicating a similar mechanism in Pt/C and the catalyst. The EIS data was fitted with the modified Randles circuit, which is shown in the inset of the figure. The pure capacitance C due to the electric double layer deviation is substituted with a constant phase element Q.

No	**Sample**	**ORR performance**				**Reference**
		Electrolyte	**Current density mA/cm^2 (1600 rpm)**	**E_{onset}/ $E_{1/2}$** (V vs RHE)	**Stability**	
1	AgCl-Ag@AgCl NWs **(**Ag-AgCl core−shell nanowires decorated with AgCl)	0.1 M KOH	4.51 mA/cm^2	0.78 V vs RHE ($E_{1/2}$)	A 10 mV change in $E_{1/2}$ after 4000 cycles of stability	10
2	One-dimensional silver halides nanowires (AgClNW)	0.1 M NaOH	AgClNW-0 −460.8 µA	1.012 V vs RHE for AgClNW-0	~87.5% reduction in current for an hour,	11
3	AgCl−SnO_2(V_O)	0.1 M NaOH	−4.1 mA/cm^2	0.78 V vs RHE	Retained the same onset potential and $E_{1/2}$, and the reduction in current density is 0.48 mA/cm^2	12
4	Dealloying in HCl performed on annealed AgCu alloy NPs	0.1 M KOH	−4.5 mA/cm^2 (1200 rpm)	0.97 V vs RHE	stability test of annealed + dealloyed Ag_7Cu_3 NPs performed at 0.8 VRHE demonstrated no significant decline	13

					in the ORR activity	
5	$Ag@Ag_2WO_4$ (Ag nanoparticle anchored Ag_2WO_4)	0.1 M KOH	-4.5	0.89 V vs RHE	After 2500 cycles retained the current density	14
6	Ag/Co_3O_4-12	1 M KOH	−5.31	0.43 NHE	Not mentioned	15
7	$AgVO_3$	0.1 M KOH	-5.22 (rpm-1800)	0.82 V vs RHE	ΔI=0.55 mA/cm^2 with a 10-mV reduction in $E_{1/2}$ potential after 2500 cycles	16
8	Silver-molybdate	1 M KOH	~ -2.0	Not mentioned	500 ADT cycles lead to a reduction in 12% of the current density of Ag–Mo-22	17
9	$Ag/Mn_3O_4/C$	0.1 M NaOH	-5.43	−0.111 V vs (MMO) ($E_{1/2}$)	Not mentioned	18
10	Ag/MoS_2	0.1 M KOH	-6	0.9 V vs RHE	good stability after 2000 cycles	19
11	$Ag/Mn_3O_4/C$	0.1 M KOH	~-5.5	0.92 V vs RHE	Not mentioned	20
12	5% Ce-MnOx/Ag	0.1 M KOH	~-5.5	~0.88 V ($E_{1/2}$)	After 5000 cycles more than 90% of their initial diffusion-limiting current densities retained	21
13	$Ag–Mn_3O_4/C$	1 M NaOH	Not mentioned	-0.11 V vs SCE	A reduction in potential of -0.41 Vs SCE after 10 h of chronoamperometric analysis	22
14	AgCl-Ag: Mn_3O_4	0.1 M NaOH	-4.2 mA/cm^2	0.844 V	$\Delta E_{1/2}$=0.002 V, and ΔI=0.22 mA/cm^2 after 2500 CV cycles and regenerable	**This work**

Table S*2*. Comparison of the ORR activity of the catalyst AgCl-Ag:Mn_3O_4 with the literature reports.

Impedance parameters	0.976 V	0.876 V	0.776 V	0.676 V	0.576 V	0.476 V	0.376 V	0.276 V
R_s (ohm)	41.51	42.3				42.79	42.98	42.99
Q-Yo	0.0001382	0.0001195				0.0001057	9.908E-5	9.417E-5
Q-n	0.7684	0.8042				0.8469	0.8554	0.8
R_P (ohm)	4.71E4	4655				4.873E4	5.014E4	1.059E4
R_s (ohm)			42.66	42.62	42.55			
Q-Yo			9.848E-5	0.000119	0.0001162			
Q-n			0.8389	0.8301	0.8332			
R_f (ohm)			2929	2705	1.674E4			
Q-Yo			0.002669	0.0004791	0.0002133			
Q-n			1	0.7638	0.873			
R_{ct} (ohm)			531.4	5290	4.76E4			

Table S3. Circuit parameters of EIS spectra of the AgCl-Ag:Mn_3O_4 in the kinetic region, mixed-diffusion region, and mass transport region.

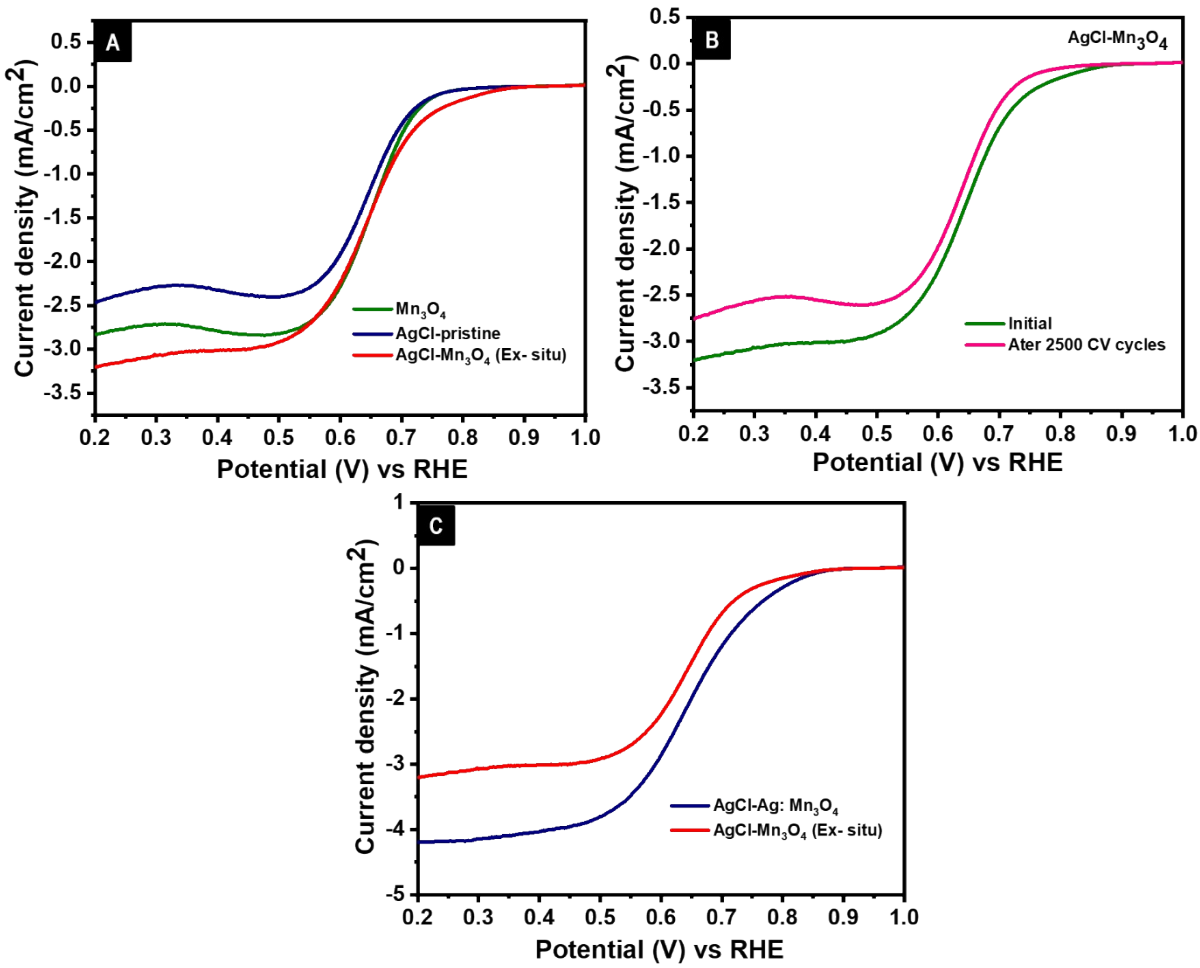

Fig. S7 LSV of pristine AgCl, Mn_3O_4, and ex-situ synthesized AgCl-Mn_3O_4 (A), ADT of AgCl-Mn_3O_4 (B), LSV of AgCl-Ag:Mn_3O_4 and two-step derived AgCl-Mn_3O_4 (C).

From Figure S7 A it is clear that the two-step derived catalyst (ex-situ) also exhibited a performance higher than the individual components AgCl, and Mn_3O_4. The onset potential obtained for the catalysts is in the order 0.824 V (AgCl-Mn_3O_4) > 0.756 V (Mn_3O_4) >0.75V (AgCl). The $E_{1/2}$ and the limiting current density obtained at 1600 rpm are in the order AgCl-Mn_3O_4 (0.63 V, -3.2 mA/cm^2) > Mn_3O_4 (0.65 V, -2.82 mA/cm^2) > AgCl (0.643 V, -2.46 mA/cm^2). It exhibited a visible shift in onset potential after ADT analysis, which is shown in figure S7 B. AgCl-Mn_3O_4 exhibited a visible change in onset potential, $E_{1/2}$, and current density ΔE_{onset}=0.061 V, $\Delta E_{1/2}$=0.004 V, and ΔI=0.44 mA/cm^2 after ADT cycles.

The two step-derived catalyst AgCl-Mn_3O_4 exhibited a lower performance than the composite synthesized via the single-step synthesis method, which is represented in Figure S7 C. These observations suggest the synergistic effect of the components resulting from the strong

interaction and the structural integrity through the simple coprecipitation reaction is responsible for the enhanced performance of the ORR catalyst. In two-step synthesis, separately synthesized AgCl and Mn_3O_4 are mixed, which can result in bulk particle formation, and maybe one component can act as support here, which altogether reduces the performance. The E_{onset}, $E_{1/2,}$ and I_{lim} of the AgCl-Ag:Mn_3O_4, AgCl-Mn_3O_4 (Two step) and the Pt/C are tabulated in Table S4. The change in E_{onset}, $E_{1/2,}$ and I_{lim} after the ADT cycles of the catalysts are also tabulated which clearly indicates the better stability of the AgCl-Ag:Mn_3O_4.

Catalyst	E_{onset} (V)	$E_{1/2}$ (V)	I_{lim} mA/cm^2	ΔE_{onset} (V)	$\Delta E_{1/2}$ (V)	ΔI_{lim} mA/cm^2
				After ADT		
AgCl-Ag:Mn_3O_4 (Single step)	0.844	0.64	-4	0.039	0.002	0.22
AgCl-Mn_3O_4 (Two step)	0.824	0.63	-3.2	0.061	0.004	0.44
Pt/C	0.941	0.79	-4.6	0.024	0.04	0.58

Table S4 E_{onset}, $E_{1/2,}$ and I_{lim} of the catalyst AgCl-Ag:Mn_3O_4, AgCl-Mn_3O_4 (Two step) and the benchmark catalyst Pt/C, after the ADT cycles.

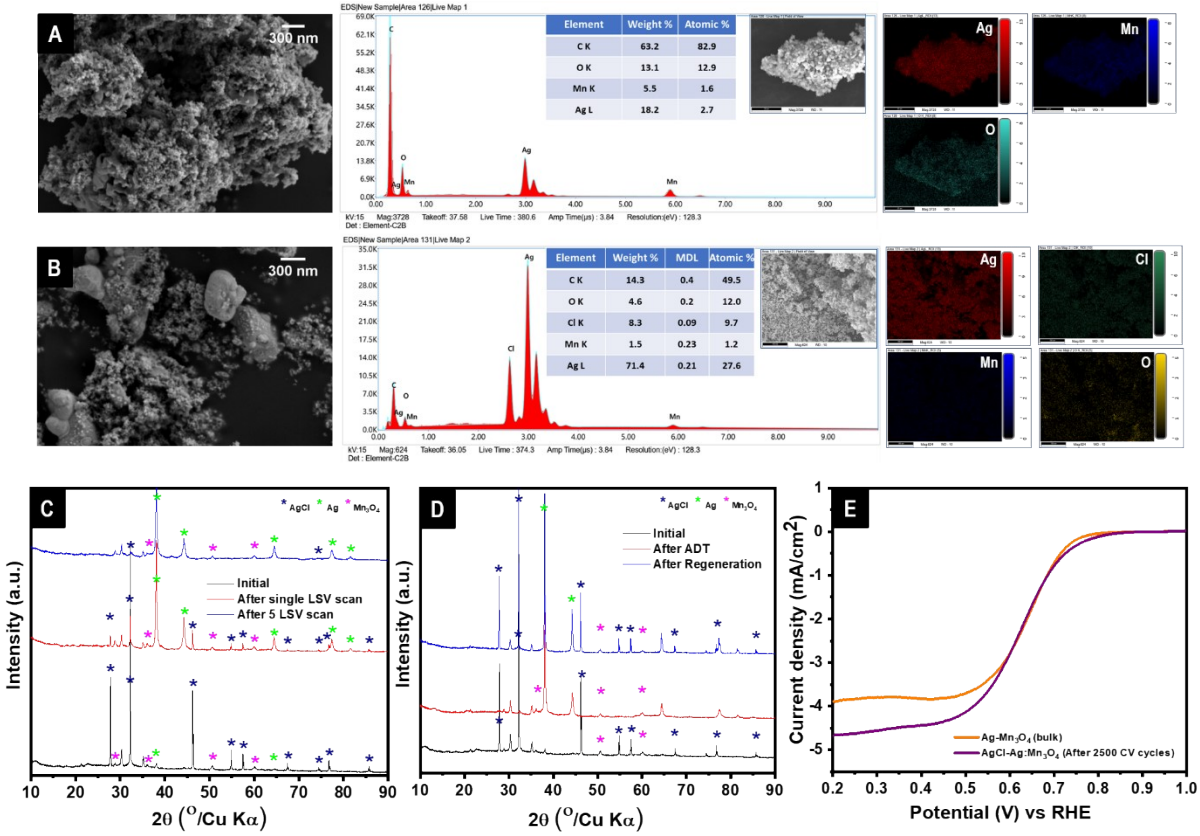

Fig. S8 SEM, EDS spectrum, and elemental mapping of AgCl-Ag:Mn_3O_4 after ADT (A), and after regeneration (B), XRD of AgCl-Ag:Mn_3O_4 after single and five consecutive LSV scans (C), before, after stability, and after regeneration (D), and LSV comparison of bulk Ag-Mn_3O_4 with after ADT AgCl-Ag:Mn_3O_4 system (E).

A slight reduction in the performance of AgCl-Ag:Mn_3O_4 system was observed after ADT, due to the conversion of AgCl to Ag in the electrochemical cycles. SEM, EDS spectrum, and elemental mapping of AgCl-Ag:Mn_3O_4 after ADT, shown in Figure S8 A confirm the conversion. The morphology changed from the layer-like structure of AgCl to nanoporous Ag. The absence of chlorine is confirmed by EDS.

Further, the regeneration of the material is done by treating the Ag-Ag:Mn_3O_4 with 0.1 M HCl. Morphological analysis was performed with SEM-EDS after ADT and regeneration. A slight change in morphology is seen in SEM and the presence of chlorine is detected in EDS after regeneration. To verify the existence of AgCl in the ORR potential, 200 µl of the catalyst ink (5 mg/ml) was drop cast on the ITO plate and structurally analyzed with XRD after single and 5 LSV scans in the potential range of 1-0.2 V. The results obtained are shown in Figure S8 C. After a single LSV scan, all the major peaks corresponding to the existence of AgCl are visible.

After 5 consecutive LSV scans, there was a reduction in AgCl peak intensity and an enhancement in the intensities of peaks of Ag. Figure S8D shows the comparison XRD of AgCl-Ag:Mn_3O_4 before, after ADT, and after regeneration on the ITO plate. The before ADT pattern exhibited all the characteristic peaks of AgCl, Mn_3O_4, and a small percentage of Ag nanoparticles. The presence of peaks at 27.7°, 32.1°, 46.2°, 54.8°, 57.4°, 67.4°, 74.4°, 76.6°, 85.6° can be assigned to the characteristic peaks of (111), (200), (220), (311), (222), (400), (331), (420), and (422) planes of cubic AgCl. The obtained data are in excellent agreement with the reported literature and JCPDS 00-031-1238. The peaks at 28.9°, 38°, 44.3°, 64.4°, and 81.5° can be assigned to tetragonal Mn_3O_4 planes (112), (004), (220), (400), and (008), respectively, and obtained result agrees with the JCPDS 01-089-4837. The XRD obtained after stability cycles on substrate-coated ITO indicated the absence of AgCl. The greater extent of silver nanoparticle formation was evidenced by the appearance of high-intensity peaks at 38.1° and 44.2° corresponding to (111) and (200) planes of Ag with JCPDS 01-089-3722. Thus, during the ADT, the catalyst AgCl-Ag:Mn_3O_4 is converted to Ag-Ag:Mn_3O_4. The complete regeneration of the material was observed after the treatment with HCl, and the material was regenerated with all the characteristic peaks of AgCl and Ag:Mn_3O_4. The uniform coating resulted in a lower contribution from the ITO plate in XRD patterns, and two small peaks from ITO are observed and represented in the figure.

On comparing the performance of Ag-Ag:Mn_3O_4 (the material after the ADT analysis) and the chemically synthesized Ag-Mn_3O_4, it was seen that the ORR activity is higher in the electrochemically converted system (Figure S8 E). This experiment further establishes the excellent ORR activity due to the formation of nanoporous Ag during the electrochemical cycle and its structural integrity with the Mn_3O_4 system, synergetically contributing to the enhanced activity.

MEA preparation

Before the MEA preparation, the PiperION® AEM membrane was kept at ambient conditions for one hour, followed by treatment with 0.5 M NaOH for one hour at room temperature. Then, the NaOH was replaced with a freshly prepared solution, the membrane was soaked further for one hour at room temperature, and the membrane was rinsed with DI water. Pt-Ru (1:1)/C was used as the anode, and the desired synthesized material was used as the cathode catalyst. 5 cm x 5 cm dimensions of GDL-coated carbon paper were used to coat the catalyst material. Catalyst ink was prepared by initially dispersing the appropriate amount of catalyst in DI water

to wet the material, followed by the addition of isopropyl alcohol and an appropriate amount of PiperION® anion exchange dispersion. The catalyst ink was coated with a paintbrush until the desired loading occurred on both anode (4.5 mg/cm^2) and cathode (4 mg/cm^2). A pressing condition of 20 kg/cm^2 was adopted to sandwich the anode-cathode catalyst-coated GDL paper and pre-treated PiperION® membrane. OCV measurements were performed with an active DMFC cell connected to an electrochemical workstation. Oxygen was purged through the cathode side, and 1 M methanol in 1 M NaOH solution was passed through the anodic compartment using a peristaltic pump at a flow rate of 1 mL/min. MEA is activated before the OCV measurement by passing methanol and oxygen through the anode and cathode compartments.[23]

Figure S9 (A-D) shows the steps involved in the preparation of MEA and its assembly in the single fuel cell. Figure S9 E shows the OCV observed for 10000 seconds. The stable OCV confirms the stability of the catalyst in the DMFC conditions.

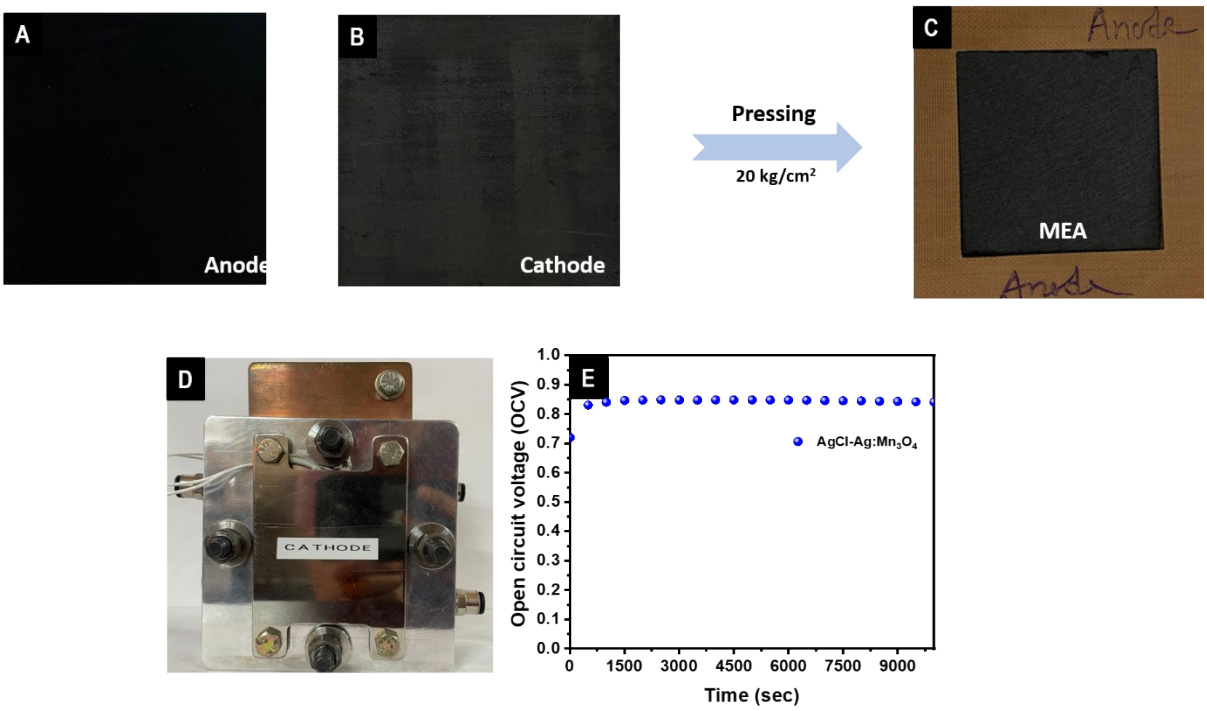

Fig. S9 Anode (A), cathode (B) catalyst-coated coated GDL paper and MEA of AgCl-Ag: Mn_3O_4 (C), a photograph of single MEA stack (D), OCV of the single stack cell during the continuous operation for10000 sec (E)

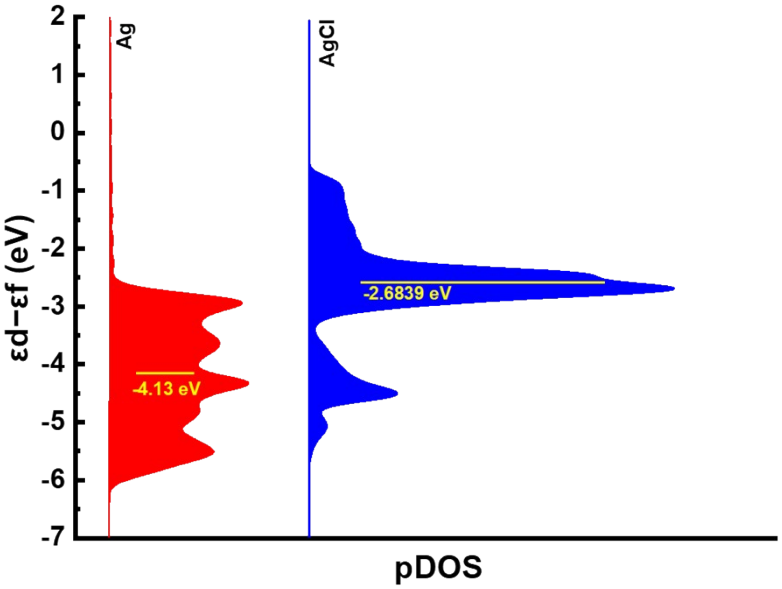

Fig. S10 pDOS of Ag and AgCl

References

1. M. Li, H. Zhang, Z. Liu, Y. Su and C. Du, *Appl. Surf. Sci.*, 2023, 268, 157302.
2. Z. Wu, K. Yu, Y. Huang, C. Pan and Y. Xie, *Chem. Cent. J.*, 2007, 1, 1–9.
3. G. S. Gund, D. P. Dubal, B. H. Patil, S. S. Shinde and C. D. Lokhande, *Electrochim. Acta*, 2013, 92, 205–215.
4. Y. Wang, C. Hou, X. Lin, H. Jiang, C. Zhang and G. Liu, *Appl. Phys. A Mater. Sci. Process.*, 2021, 127, 1–7.
5. Y. Wang, J. Hao, W. Li, X. Zuo, B. Xiang, Y. Qiang, X. Zou, B. Tan, Q. Hu and F. Chen, *J. Mater. Sci.*, 2020, 55, 724–737.
6. M. M. Mohamed and H. El-Farsy, *Sci. Rep.*, 2020, 10, 1–18.
7. S. S. Acharyya, S. Ghosh, S. K. Sharma and R. Bal, *RSC Adv.*, 2015, 5, 89879–89887.
8. J. Liu, J. Liu, W. Song, F. Wang and Y. Song, *J. Mater. Chem. A*, 2014, 2, 17477–17488.
9. D. Lan, M. Qin, R. Yang, H. Wu, Z. Jia, K. Kou, G. Wu, Y. Fan, Q. Fu and F. Zhang, *J. Mater. Sci. Mater. Electron.*, 2019, 30, 8771–8776.

10. S. Choi, Y. Park, J. Choi, C. Lee, H. S. Cho, C. H. Kim, J. Koo and H. M. Lee, *ACS Sustain. Chem. Eng*., 2021, 9, 7519–7528.

11. S. jin Kim, S. C. Lee, C. Lee, M. H. Kim and Y. Lee, *Nano Energy*, 2018, 48, 134–143.

12. A. Yatheendran, R. Rajan and N. Sandhyarani, *Langmuir*, 2023, **39**, 11708–11719.

13. T. Balkan, H. Küçükkeçeci, D. Aksoy, M. Harfouche, Ö. Metin and S. Kaya, *Sustain. Energy Fuels*, 2022, 6, 2593–2601.

14. K. Nubla and N. Sandhyarani, *Electrochim. Acta*, , DOI:10.1016/j.electacta.2020.135942.

15. A. Ashok, A. Kumar, M. A. Matin and F. Tarlochan, ACS Omega, 2018, 3, 7745–7756.

16. K. Nubla, M. F. Puthiyaparambath, R. Chatanathodi and N. Sandhyarani, *Mater. Chem. Front*., 2022, 6, 2042–2050.

17. Y. Wang, Y. Liu, X. Lu, Z. Li, H. Zhang, X. Cui, Y. Zhang, F. Shi and Y. Deng, *Electrochem. commun*., 2012, 20, 171–174.

18. Q. Tang, L. Jiang, J. Qi, Q. Jiang, S. Wang and G. Sun, *Appl. Catal. B Environ*., 2011, 104, 337–345.

19. S. V. Prabhakar Vattikuti, P. C. Nagajyothi, K. C. Devarayapalli, K. Yoo, N. Dang Nam and J. Shim, *Appl. Surf. Sci*., 2020, 526, 1–9.

20. S. A. Park, H. Lim and Y. T. Kim, *ACS Catal*., 2015, 5, 3995–4002

21. W. Wang, J. Q. Chen, Y. R. Tao, S. N. Zhu, Y. X. Zhang and X. C. Wu, *ACS Catal*., 2019, 9, 3498–3510.

22. J. Liu, J. Liu, W. Song, F. Wang and Y. Song, *J. Mater. Chem. A*, 2014, 2, 17477–17488.

23. T. Palaniselvam, V. Kashyap, S. N. Bhange, J. B. Baek and S. Kurungot, *Adv. Funct. Mater.*, 2016, 26, 2150- 2162.